

# Adversarially Learning a Local Anatomical Prior: Vertebrae Labelling with 2D reformations

Anjany Sekuboyina<sup>†</sup>, Markus Rempfler, Alexander Valentinitch, Jan S. Kirschke\*, and Bjoern H. Menze\*

**Abstract**—Robust localisation and identification of vertebrae, jointly termed *vertebrae labelling*, in computed tomography (CT) images is an essential component of automated spine analysis. Current approaches for this task mostly work with 3D scans and are comprised of a sequence of multiple networks. Contrarily, our approach relies only on 2D reformations, enabling us to design an end-to-end trainable, standalone network. Our contribution includes: (1) Inspired by the workflow of human experts, a novel butterfly-shaped network architecture (termed *Btrfly net*) that efficiently combines information across sufficiently-informative sagittal and coronal reformations. (2) Two adversarial training regimes that encode an anatomical prior of the spine’s shape into the *Btrfly net*, each enforcing the prior in a distinct manner.

We evaluate our approach on a public benchmarking dataset of 302 CT scans achieving a performance comparable to state-of-art methods (identification rate of >88%) without any post-processing stages. Addressing its translation to clinical settings, an in-house dataset of 65 CT scans with a higher data variability is introduced, where we discuss refinements that render our approach robust to such scenarios.

**Index Terms**—vertebrae detection and localisation, computed tomography, fully-convolutional networks, prior-encoding, anatomical prior, adversarial learning.

## I. INTRODUCTION

The spinal column is the central load-carrying structure in the human body, connecting the head with the pelvis. It contributes to the posture of the body ensuring the healthy functioning of the organ systems. Spinal pathologies can have catastrophic consequences, for example, osteoporotic fractures are associated with an 8-fold higher mortality rate in the long-term [1]. In Europe, chronic lower back pain is the most prevalent cause of disability in young adults [2]. Despite this, spinal pathologies are frequently missed in routine imaging; in particular, vertebral fractures are frequently overlooked [3]. Thus, there exists a need for an algorithmic intervention in spinal images that supports an expert in making an informed diagnosis. A significant part of such an algorithm would deal with localisation and identification of spinal structures such as vertebrae, intervertebral discs, and the spinal cord, followed by analysing their structure. In this work, we focus on labelling the vertebrae, which is the joint task of locating and identifying the cervical, thoracic, lumbar, and sacral vertebrae in a regular

CT spine scan. Labelling the vertebrae has immediate diagnostic consequences, e.g: vertebral landmarks help identify structural deformities in the spine such as scoliosis or pathological lordosis and kyphosis. From a modelling perspective, the vertebrae labelling task simplifies the downstream tasks of intervertebral disc segmentation or vertebral segmentation. These landmarks can be also employed in 3D modelling of the spine for for surgical planning or its bio-mechanical modelling for load analysis.

For such an endeavour, it is important to appreciate the challenges involved. The size of a full spine scan, typically exceeding  $10^7$  voxels, poses severe computational restrictions for processing it in its entirety. There also exists a wide variation in the field-of-views (FOV) of these scans, which requires an algorithm for detecting landmarks to be robust to key-point identification. Added to this is the high correlation in the shape of various vertebrae and the abnormalities prevalent in the scans such as of spinal deformities, vertebral fractures, and insertions. Fig 1a shows a sample of the scans the algorithm has to deal with, which illustrate the robustness required of any automated approach.

### A. Related work

Our attempt at designing a prior-encoded vertebrae labelling algorithm is primarily motivated by two major factions: vertebrae labelling and prior learning. Here, we present the relevant literature segregated into these fields.

**Vertebrae labelling.** The approaches aimed at labelling broadly fall into two factions, a more traditional model-based approaches and relatively recent learning-based ones. Model-based approaches like [4], [5], and [6] relied on prior information about the spine’s structure, usually as statistical shape models or atlases, for identifying the vertebrae. Due to their extensive reliance on priors, their generalisability was limited. From a machine learning perspective, one of the incipient and notable works by Glocker et al. [7], followed by [8] used context-based features with regression forests and Markov models for labelling. On a similar footing, [9] proposed a deep multi-layer perceptron using long-range context features. In spite of their intuitive motivation, these approaches suffer a setback in case of limited FOVs or abnormal cases (e.g: metal insertions, contrast) due to their use of hand-crafted features. With the emergence of convolutional neural networks (CNN), Chen et al. [10] proposed a joint-CNN as a combination of a random forest for initial candidate selection followed by a CNN trained to identify the vertebra based on its appearance and a conditional dependency on its neighbours. Without hand-crafting the features, this approach performed remarkably well.

A. Sekuboyina is with the Department of Informatics, Technical University of Munich, Germany and Department of Neuroradiology, Klinikum rechts der Isar, Germany. e-mail: anjany.sekuboyina@tum.de

M. Rempfler and B. H. Menze are with Department of Informatics, Technical University of Munich, Germany.

A. Valentinitch and J. S. Kirschke are with Department of Neuroradiology, Klinikum rechts der Isar, Germany.

<sup>†</sup>Corresponding author. \*Joint supervising authors.

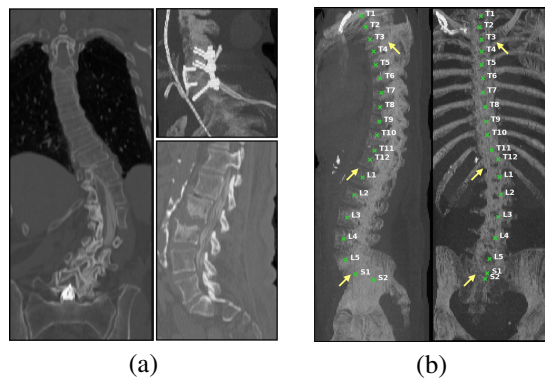


Fig. 1: (a) Example spine scans indicating the variability that exists in the images. (b) Sagittal and coronal maximum intensity projections of a spine CT highlighting a few markers human experts use in order to label the vertebrae.

However, since the CNN works on a limited region around the vertebra, it results in a high variability of the localisation distance. Recently, Yang et al., with [11] and [12], proposed a deep, volumetric, fully-convolutional 3D network (FCN) called DI2IN with deep-supervision posing the labelling task as a regression problem. The output of DI2IN is improved in subsequent stages that employ either message-passing across channels or an recurrent neural network (specifically, a convolutional LSTM) followed by further tuning with a shape dictionary. Very recently, Liao et al. [13], motivated by the *sequence* in the vertebral order, proposed a similar combination of a convolutional and a recurrent neural network. This approach, along with its recent predecessors, deserve credit for tackling the problem of labelling by exploiting the representational capability of deep networks while attempting to incorporate prior knowledge about the spine scan. Such a combination becomes imperative because an FCN does not necessarily learn the anatomy of a region-of-interest especially when working in 3D as the depth of the network is constricted by its computational complexity. This is a severe limitation particularly because human-equivalent learning augments anatomical information with prior knowledge for an accurate performance.

**Prior & adversarial learning in CNNs.** Recent work in [14] propose encoding (anatomical) segmentation priors into an FCN by learning the shape representation using an auto encoder (AE) alongside the primary segmentation network. The AE once trained projects a new prediction onto the space of the learnt, true segmentations, thus repeating the ‘shape’. Different from this, in [15], the encoder of a similarly pre-trained AE is used to provide projection-loss (euclidean distance in latent space) to train the primary network.

Notice the parallels that can be drawn between these prior encoding approaches and generative adversarial networks (GAN) [16],[17]. Both of them have two networks, a primary network ( $\sim$ generator) generating a prediction and an auxiliary auto-encoding network ( $\sim$ discriminator) working on the *goodness* of this prediction. Architecturally closer to the AE-like secondary network is the energy-based GAN proposed by Zhao et al. [18] that uses an AE as a discriminator and its reconstruction energy as the adversarial signal.

## B. Our contribution.

Instead of working with volumetric data, we propose an architecture that makes use of *appropriate* 2D projections for labelling the vertebrae, referred to as the ‘Btrfly’ architecture. By doing so, our approach can work on high resolution data and does not suffer the computational bottlenecks of its counterparts. Fig. 1b shows sagittal and coronal maximum intensity projections of a scan highlighting some of the key markers used by human-experts for labelling the vertebrae.

Underpinning this architecture, and motivated by the equivalence of prior-learning methods and GANs, we propose an adversarial training regime that learns an anatomical prior of the spine and encodes it into the Btrfly net. Significantly differing from previous prior-encoding approaches: (1) We do not *pre-train* the auxiliary networks on ground truth annotations to learn an appropriate latent space. Rather, they are adversarially trained in tandem with the labelling network, (2) our problem is more akin to landmark localisation than to segmentation, which requires a redefinition of the notion of an anatomical *prior*, and lastly (3) we explore two different adversary architectures for enforcing the prior. Of special interest to us are energy-function based adversaries [18] and Wasserstein-distance based adversaries [17]. We believe that an adversary offering an anatomically-inspired supervision instead of the usual binary adversarial supervision is more effective for medical imaging tasks where the data is limited and the variation across anatomical images is not as diverse as in natural images.

In summary, improving on our previous work [19], we propose an end-to-end solution for vertebrae labelling by adversarially training an FCN, thereby encoding the local spine structure into it. More precisely, we present:

- A butterfly-shaped network architecture for labelling the vertebrae in 3D while operating on the sufficiency of certain 2D sagittal and coronal reformations by combining information across these views at a large receptive field.
- An adversarial training regime for encoding spine’s structural anatomy into the labelling network using two prominent adversary architectures: the energy-based adversarial AE and the Wasserstein-distance based discriminator. We also present an analysis of *how* adversarially learning the prior improves labelling performance by probing the latent spaces of the labelling networks with and without encoding.
- An comprehensive evaluation of the various components of our approach (the architecture, adversarial encoding etc.) on two datasets: (i) a public dataset of 302 CT scans on which the performance of our approach is comparable to the current state-of-art, with the advantage of being completely end-to-end and computationally lean and (ii) an in-house dataset of 65 CT scans on which we test our approaches’s generalisability. As part of this, we introduce a pre-processing stage for spine localisation that enables our approach to generalise out-of-box to clinical settings by subduing the variability in any data.

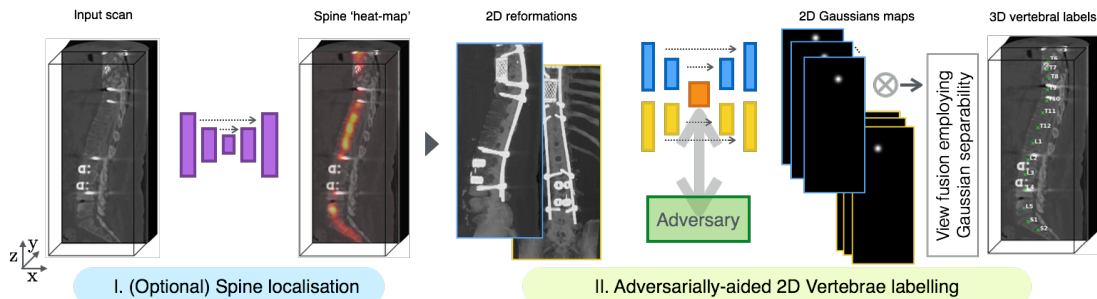


Fig. 2: An overview of our labelling approach. Also illustrated is the spine localisation stage which is, in some cases, necessary for our approach to be generalisable to any clinical CT scan.

## II. METHODOLOGY

We present our approach in three stages: First, motivating the characteristics of two-dimensional projections in spinal CT images, we introduce the *butterfly* architecture for labelling. Second, we detail two variants of adversarial training that enable learning the spinal shape as a prior, thereby encoding it into the labelling network. Finally, we present our inference process for obtaining 3D labels from our 2D predictions. An overview of our approach is illustrated in Fig. 2.

### A. Butterfly Network

At the outset, a fully-convolutional, 3D CNN can be employed to regress on the vertebral labels. But, note that the task of localisation and identification requires large context to work with so as to capture distant key-points or markers (cf. Fig. 1b). Collating information from such distant markers requires a network with a considerably large receptive field, or analogously, a deeper network. Working on volumetric data with such networks poses severe computational restrictions that are often dealt with by subsampling the spatial resolution significantly or working on sub-images as in [10]. But, this comes at the cost of losing critical spatial information, e.g. intervertebral discs or vertebral posteriors. On the contrary, working in two dimensions is computationally favourable, making model design easier for limited data. But, transitioning from 3D to 2D comes with an enormous loss of information. It is therefore desirable to make this transition in an intelligent, task-dependent manner.

Taking into consideration the anatomy of the spine, we hypothesise that working with *sufficiently* representative, 2D projections of the volumetric data is a viable alternative for labelling the vertebrae. This readily removes the computational restriction described above. Since 2D data is significantly lighter in terms of storage and processing loads, we can work at higher scan resolutions and can design deeper networks with improved representational capacities. It is, however, important to choose an appropriate projection depending on the task. As we work with bone, we employ sagittal and coronal maximum intensity projections (MIP). The former captures the spine’s curve and the sacral and cranial bones while the latter captures the rib-vertebrae joints and the hip bones, all of which are crucial markers for labelling. Note that a naive MIP might not always be the optimal choice, eg. in full-body scans the ribcage

obstructs the spine in a MIP. For such cases, we introduce a pre-processing stage of spine localisation that is employed to remove these occlusions, and is discussed in section IV.

1) *Notation*: We denote a 3D scan by  $\mathbf{x} \in \mathbb{R}^{h \times w \times d}$ , where  $h$ ,  $w$ , and  $d$  are the height, width, and depth of the scan respectively. In the training phase, we have annotations of the form  $\mu_i \in \mathbb{R}^3$  ( $i \in \{1, 2, \dots, 26\}$ ) denoting the location of the  $i^{\text{th}}$  vertebra. From such annotations, a 27-channelled, 3D map is constructed and denoted by  $\mathbf{y} \in \mathbb{R}^{h \times w \times d \times 27}$ . Except the background channel  $y_0$ , each of  $\mathbf{y}$ ’s twenty six channels correspond to the 26 vertebrae (C1 to S2). In each channel, the vertebrae’s position is marked by a Gaussian heat map. Formally,  $y_i = e^{-\|\mathbf{x} - \mu_i\|^2 / 2\sigma^2}$  constructs the  $i^{\text{th}}$  channel with  $\sigma$  controlling the spread of the Gaussian.  $y_0$  is then constructed as  $1 - \max_i(y_i)$  at every voxel. During inference, we intend to predict this  $\mathbf{y}$  from which the vertebral locations can be extracted. We denote the sagittal and coronal projections of  $\mathbf{x}$  and  $\mathbf{y}$  with  $\mathbf{x}_{\text{view}}$  and  $\mathbf{y}_{\text{view}}$ ,  $\text{view} \in \{\text{sag}, \text{cor}\}$ . The dimensions of  $\mathbf{x}_{\text{sag}}$  and  $\mathbf{y}_{\text{sag}}$  are  $(h \times w)$  and  $(h \times w \times 27)$  respectively, and can be similarly deduced for the other view.

2) *Architecture*: The problem of learning the vertebrae labels is formulated as multi-variate regression task, learning a mapping  $G$  from projections to label maps,  $G : \{\mathbf{x}_{\text{sag}}\} \times \{\mathbf{x}_{\text{cor}}\} \mapsto \{\mathbf{y}_{\text{sag}}\} \times \{\mathbf{y}_{\text{cor}}\}$ .  $G$  is also synonymous to a *generator*, as introduced in subsequent sections. Taking cues from the ubiquitous U-architectures, we cast  $G$  as a 2D FCN. From Fig. 1b, observe that the spine is spatially overlapping in the two projections and there exists useful markers in both the sagittal and coronal projections. This motivates a joint processing of both the views, which can be achieved by employing a butterfly-like FCN. Illustrated in Fig. 3, it has two arms (xy- and xz-), one for each projection. After three layers of initial processing, the weights of both the arms are concatenated and their combination is further processed. The network thus learns the inter-dependency and the relative importance of both the views depending on the input. Additionally, we employ skip-connections for better gradient flow, batch normalisation after every convolution, and ReLUs as non-linearities. We refer to this network as the ‘Btrfly’ net.

Note that for an eventual concatenation of sagittal and coronal weight maps, the dimensions  $w$  and  $d$  should be equal (since, by construction,  $h$  is common in both views). We observed that on the datasets we worked with, centre padding the smaller dimension sufficed when necessary.

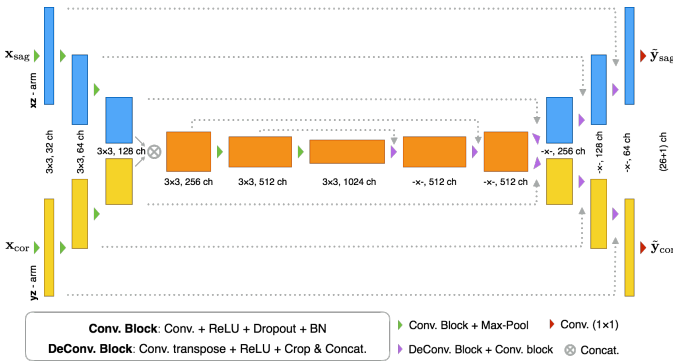


Fig. 3: The Btrfly architecture. The xz- (blue) and the yz-arms (yellow) correspond to the sagittal and coronal views. In the upscaling path, the kernel size  $- \times -$  denotes to two different kernel sizes:  $4 \times 4$  transposed convolution followed by  $3 \times 3$  convolution.

3) *Loss*: For training the Btrfly net, an  $\ell_2$  distance is chosen as the primary loss supported by a cross-entropy loss over the softmax excitation of the ground truth and the prediction. Jointly, they control the ‘Gaussian-ness’ of the label maps and the spatial ordering of these Gaussians across the twenty seven channels respectively. We observed that the former dominates in initial epochs of training while the latter takes over towards convergence. The loss for one arm is expressed as:

$$\mathcal{L}_{b,sag} = \|\mathbf{y}_{sag} - \tilde{\mathbf{y}}_{sag}\|_2 + \omega H(\mathbf{y}_{sag}^\sigma, \tilde{\mathbf{y}}_{sag}^\sigma), \quad (1)$$

where  $\tilde{\mathbf{y}}_{sag}$  is the prediction of the net’s xz-arm,  $H$  is the cross-entropy function, and  $\mathbf{y}_{sag}^\sigma = \sigma(\mathbf{y}_{sag})$ , the softmax excitation of the prediction.  $\omega$  is the median frequency weight map over the occurrence of vertebral labels, incorporated for boosting the learning of less frequent vertebral classes. The loss for the yz-arm is similarly constructed resulting in the total loss of the Btrfly net:  $\mathcal{L}_{btrfly} = \mathcal{L}_{b,sag} + \mathcal{L}_{b,cor}$ .

### B. Adversaries for local prior encoding

In the case of vertebral labels, a one-to-one mapping between the order and the location of the vertebrae is a strong prior, e.g. L2 is always below L1 and above L3 (notwithstanding spinal deformities). However, it is not straightforward to feed this information into a neural network. This is because the voxel-level predictions of an FCN are independent of each other owing to the spatial invariance of convolutions, albeit related through receptive field and overlap of transposed convolutions. Consequently, an FCN need not necessarily learn the anatomical prior. Therefore, in earlier approaches for vertebrae labelling, a subsequent *correction step* was implemented based on a learnt dictionary [11], or a second network was tasked with enforcing the spatial sequence across the vertebral labels [12], [13]. We propose to impose this anatomical prior of the spine’s shape into our primary network by *adversarially* encoding the spine’s local geometric shape.

1) *Formulation & Notation*: Recall that the label maps,  $\mathbf{y}_{view}$ , consist of a 2D Gaussians at the vertebral location in each channel (except  $y_0$ ). Processing the 2D-channelled  $\mathbf{y}_{view}$  as a 3D volume lets us learn the spatial spread of Gaussians across channels and consequently the vertebral labels. As we

are concerned only with the spatial spread of the vertebrae, we exclude the background channel ( $y_0$ ) for adversarial learning. Thus,  $\mathbf{y}_{view}$  (or  $\tilde{\mathbf{y}}_{view}$ ) in this section are 26-channelled 2D images that are processed as 3D volumes.

We denote the generator (viz. Btrfly) and discriminator networks by  $\mathbf{G}$  and  $\mathbf{D}$  and their corresponding function mappings by  $G$  and  $D$ , respectively. Following is a description of two families of adversaries: energy-based discriminators (EB-D) and Wasserstein distance-based discriminators (W-D), both encoding the prior in distinct ways. Fig. 4a shows the arrangement of the discriminators with respect to the Btrfly.

2) *Energy-based adversary*: An auto encoder (AE) is an obvious tool for learning a latent space that best represents the spatial distribution of the vertebral labels. However, as there exists extreme variability in FOV of spine scans (i.e., not all vertebral labels are always present in annotations), the shape of spine and all its partial appearances need to be learnt. This is challenging owing to limited data. Moreover, learning one prior for the entire spine makes its incorporation to partial spines not trivial, requiring additional steps of registration or shape-matching [5]. It is therefore preferable to learn the spatial spread of the vertebrae *in parts*. Put differently, we learn the *local* spread of vertebrae. For this, we employ a fully-convolutional, 3D AE with a receptive field covering a part of the spine at a time. Different from conventional prior-learning approaches, we do not pre-train this AE, but train it adversarially alongside the Btrfly network.

*Overview*. As a remedy for mode-collapse and instability observed in min-max GAN [16], Zhao et al. [18] proposed to use an energy-based adversarial formulation. In this, the adversarial signal not a probabilistic signal but an energy signal. The discriminator design involves an AE that is trained to assign low energy (or reconstruction error) to an input from a real distribution and vice versa. We adapt this setup into our adversarial training owing to its geometric motivation.

*Architecture*. Our 3D adversary is fully-convolution by design (cf. Fig. 4b). Therefore, scans can be processed at their true resolution without resizing to fixed dimensions as would be needed for AE with fully-connected layers. This facilitates its joint training with the Btrfly. The adversary is a functional predicting the  $\ell_2$  distance between the input  $\mathbf{y}_{view}$  (or  $\tilde{\mathbf{y}}_{view}$ ) and its reconstruction,  $rec(\mathbf{y}_{view})$ :  $D(\mathbf{y}_{view}) = E = \|\mathbf{y}_{view} - rec(\mathbf{y}_{view})\|_2$ . This energy,  $E$  is fed back into  $\mathbf{G}$  for adversarial supervision. We improve upon  $\mathbf{D}$ ’s architecture proposed in [19] by increasing both its representational capacity and its receptive field. All the encoding convolutional layers are followed by drop-out layers with a retaining probability of 0.8. This architecture results in a spatial receptive field of  $128 \times 128$  pixels. At an isotropic resolution of 2 mm, this covers about 4 lumbar vertebrae and more elsewhere.

*Loss*. As in any adversarial setup, EB-D is shown real ( $\mathbf{y}_{view}$ ) and generated annotations ( $\tilde{\mathbf{y}}_{view}$ ) and is encouraged to accurately reconstruct the real annotations, thereby resulting in low  $E$ . On the other hand,  $\mathbf{G}$  learns to generate ‘real-looking’ annotations that would result in a lower  $E$  when passed through EB-D. For a given positive, scalar margin  $m$ ,

the following generator and discriminator losses are optimised:

$$\mathcal{L}_D = D(\mathbf{y}_{\text{view}}) + \max(0, m - D(\tilde{\mathbf{y}}_{\text{view}})), \text{ and} \quad (2)$$

$$\mathcal{L}_G = D(\tilde{\mathbf{y}}_{\text{view}}) + \mathcal{L}_{\text{b,view}}. \quad (3)$$

The joint optimisation of (2) and (3) for both the EB-Ds results in a  $\mathbf{G}$  that performs vertebrae labelling while respecting the spatial distribution of the vertebrae across channels.  $m$  is decayed to 0 as the training proceeds, where the setup attains the Nash equilibrium. Its initial positive value explicitly discourages  $\mathbf{D}$  from reconstructing  $\tilde{\mathbf{y}}_{\text{view}}$ . We refer to this prior-encoded  $\mathbf{G}$  as the **Btrfly**<sub>pe-eb</sub> net.

3) *Wasserstein distance-based adversary*: Alongside auto-encoder based adversaries exists another category of adversaries that do not involve any reconstruction, eg. min-max GAN’s discriminator [16] that predicts a probability value, or the one in Wasserstein GAN [17], [20] that predicts a real number. These discriminators contain only a contracting encoder. Here, we adapt a stable modification of the Wasserstein GAN’s [20] adversarial setup to work with Btrfly net. Since  $\mathbf{W-D}$  encodes the entire input into one scalar value for adversarial supervision, the notion of encoding *local* prior does not hold. Therefore, it is of special interest to us to compare such a *global* encoding scheme to a local, geometrically-inspired, energy-based adversarial scheme.

**Overview.** Min-max GANs typically learn by minimising the Jensen-Shannon (JS) divergence or the Kullback-Leibler (KL) divergence. [17] argues that these divergences are non-continuous especially when the support of the data distribution has minimal overlap with that of the generation’s distribution, leading to non-differentiability or sparse gradients. As an alternative, the authors propose to minimise the Wasserstein distance or the Earth Mover’s (EM) distance, which is continuous under certain assumptions. We refer the reader to [17], [20], and [21] for a detailed description of Wasserstein GAN.

**Architecture.** As  $\mathbf{W-D}$  maps an image to a real number, we have a contracting encoder followed by dense connections and no sigmoid at the end. We retain the encoding part of EB-D with minor modifications. The average pooling layers and dilated convolutions in EB-D’s encoder are replaced with strided convolutions so as to avoid sparse gradients. Working with varying FOVs implies that the dimensions of the last convolution block varies across scans. Therefore, directly plugging-in dense layers becomes challenging. To alleviate this, we employ a spatial pyramid pooling (SPP) layer [22] that chooses appropriate pool-strides and -sizes in order to map an input of varying size to an output vector of fixed length. The choice of the region to pool over depends on the application. In our case, we choose pool levels of 3 and 4 in order to retain already encoded parts of the spine. This results in a 1820-length vector that is mapped to the discriminator’s output. The detailed structure of  $\mathbf{W-D}$  is shown in Fig. 4c and this prior-encoded  $G$  is referred to as the **Btrfly**<sub>pe-w</sub> net.

**Loss.** Our loss function adapts training regime of the improved Wasserstein GAN with gradient penalty [20]. The combined setup of the  $\mathbf{G}$  and  $\mathbf{D}$  tries to minimise the Wasserstein distance between the distributions of real and generated

annotations. Incorporating its Kantorovich-Rubinstein dual (cf. theorem 3 in [17]), the WGAN’s objective is represented as:

$$\min_{\mathbf{G}} \max_{\mathbf{D}} \mathbb{E}_{x \sim \mathbb{P}_{\mathbf{y}_{\text{view}}}} [D(x)] - \mathbb{E}_{x \sim \mathbb{P}_{\tilde{\mathbf{y}}_{\text{view}}}} [D(x)], \quad (4)$$

where  $\mathbb{P}$  denotes probability distribution and  $D$  belongs to a set of 1-Lipschitz function. To satisfy this constraint on  $D$  and to smooth the gradients over different generations, a regularisation term is added that penalises the gradients across generations for variations. Splitting (4) according the parameters of  $\mathbf{D}$  and  $\mathbf{G}$  being optimising results in the loss functions below:

$$\mathcal{L}_D = D(\tilde{\mathbf{y}}_{\text{view}}) - D(\mathbf{y}_{\text{view}}) + \lambda(\|\nabla_{\tilde{\mathbf{y}}_{\text{view}}} D(\tilde{\mathbf{y}}_{\text{view}})\|_2 - 1)^2 \text{ and} \quad (5)$$

$$\mathcal{L}_G = -D(\tilde{\mathbf{y}}_{\text{view}}) + \mathcal{L}_{\text{b,view}}, \quad (6)$$

where  $\hat{\mathbf{y}}_{\text{view}} = \epsilon \mathbf{y}_{\text{view}} + (1 - \epsilon) \tilde{\mathbf{y}}_{\text{view}}$ , for any  $\epsilon \sim U[0, 1]$ . Note that the authors in [20] propose to use layer normalisation instead of batch normalisation so as to not disturb the *per sample* statistics. However, we observed that using batch normalisation gave us better results. This could be due to our data being relatively uniform and similar (label masks between 0 and 1) and a small batch size. Alternating optimisation of (5) and (6) results in an encoded  $G$ .

Owing to  $\mathbf{W-D}$ ’s architecture which outputs one real number per input sample, the encoding is no longer *local*. Each element of the encoder’s last convolution layer a certain local spread of the vertebrae, which is then passed through a dense layer resulting in *global* encoding.

### C. Inference

Once trained, inference for a given input scan of size  $(h \times w \times d)$  proceeds as: the desired sagittal and coronal MIPs are obtained and fed to the corresponding arms of the Btrfly net. Note that the discriminator (EB-D or  $\mathbf{W-D}$ ) is no longer included during inference. Its role of encoding the prior into the Btrfly net ends with the convergence of adversarial training. The Btrfly net produces a sagittal heatmap of dimension  $(h \times w \times 27)$  and coronal heatmap of dimension  $(h \times d \times 27)$ . At this stage, we define a threshold,  $T$ , the values below which are zeroed out, thus removing noisy predictions. An outer product of the predictions results in the final 3D heatmap as  $\tilde{\mathbf{y}} = \tilde{\mathbf{y}}_{\text{sag}} \otimes \tilde{\mathbf{y}}_{\text{cor}}$ , where  $\otimes$  denotes an outer product. The 3D locations of the vertebral centroids are then obtained as the locations of the maxima in their corresponding channels.

Not all vertebrae are always visible in a scan. Therefore, it is important to appropriately mark a non-zero response in a certain channel as a valid prediction or regression noise. This is done by  $T$ , allowing it to regulate false positive labels. Unless explicitly mentioned, we set  $T = 0$ . However, its value can be chosen on the validation set based on the performance measure of interest. A detailed analysis on varying values of  $T$  is presented in section III-E.

## III. EXPERIMENTS: ABLATIVE BENCHMARKING

In this section, we present a series of experiments evaluating the contribution of two key components of our approach: the

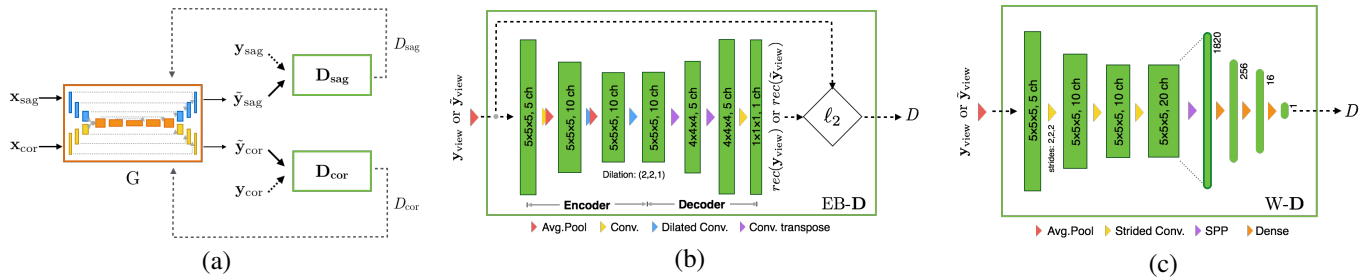


Fig. 4: (a) The arrangement of the discriminators with respect to the Btrfly net. (b) The composition of the energy-based discriminator (EB-D), giving an  $\ell_2$  reconstruction error as output. (c) The architecture of the Wasserstein-distance-based discriminator (W-D). In both the architectures, Leaky ReLU and batch normalisation is employed after every layer except the last.

Btrfly architecture and the two adversarial training schemes. We also present an analysis of the latent spaces pertaining to our network variants so as to understand how prior-encoding aids learning and improves performance.

### A. Implementation & evaluation details

1) *Dataset*: We work with a dataset released as part of the vertebrae localisation and identification challenge of the Computational Spine Imaging (CSI) workshop in MICCAI 2014. For brevity, we henceforth refer to this dataset as  $CSI_{label}$ . First introduced in [8], the dataset consists a total of 302 CT scans (242 for training and 60 for testing) with diverse FOVs. It is also rife with challenging artefacts such as scoliotic spines, and metal insertions as shown in various illustrations spread across this work.

2) *Data preparation*: As part of intensity normalisation, the extreme negative values outside the FOV (but within the scan) are clipped at -1000, corresponding to the Hounsfield unit (HU) value of air. The data is resampled to a 2 mm isotropic resolution. Recall that we work with sagittal and coronal MIPs. Since the  $CSI_{label}$  dataset is centred around spine, a naive MIP typically suffices as it is not occluded by the rib cage. In order to enhance the network’s robustness to localisation error and scan noise, data is augmented by taking ten projections from every scan. For each projection,  $n$  slices of interest are considered where  $n \sim U[d/2, d]$  for a sagittal projection and  $n \sim U[w/2, w]$  for a coronal one. This results in a training size of 2420 images. During the test phase, however, a simple MIP is performed across all the slices along the two views.

3) *Training*: Of the 242 scans for training, ten scans are held out for validation. For training, an Adam optimiser is employed with an initial learning rate of  $\lambda = 1 \times 10^{-3}$ .  $\lambda$  is decayed by a factor of 3/4th every 10k iterations to  $0.2 \times 10^{-3}$ . The learning rate of the discriminator also follows the same initialisation and decay rule. All the network variants are trained for 80k iterations and convergence is confirmed on validation set. Data is further augmented on-the-fly using translation ( $\pm 10$  pixels), rotation ( $\pm 5$  deg), and scaling (0.8–1.2 $\times$ ) operations. For every update of  $G$ ,  $D$  is updated once. Since our generator receives useful gradients from the primary loss function ( $\mathcal{L}_{btrfly}$ ) from the start of training, we did not have to use a different update interval for  $G$  and  $D$  or a two time-scale update rule (TTUR) as is normally the case for purely generative applications.

4) *Evaluation metrics*: For evaluating the performance of our network, we use two metrics defined in [7] namely, *identification rate* (id. rate) and *localisation distance* ( $d_{mean}$  &  $d_{std}$ ). Table I lists the performance our networks and compares it with prior work. In order to be agnostic to initialisation, we report the mean performance over three runs of training with independent initialisations.

### B. Contribution of Btrfly architecture

So as to validate the importance of combining the views and processing them in the Btrfly net, we compare it’s performance to a network setup working individually on the views without any such combination of weights. This setup is denoted as Cor.+Sag. network. The architecture of each of these networks is similar to one arm of the Btrfly net without feature concatenation before the bottleneck, leading to a halved number of filters in each of the bottleneck layers. Please note that the total number parameters in this setup is equal to the Btrfly net. In Table I, observe an improvement in performance due to the combination of views in the Btrfly net. Also note the reduction in variance of the localisation distances. This can be attributed to two reasons: first, the obvious advantage that one view gets from the key points in the other and second, the combination of views causes the predictions of the Btrfly net to be spatially consistent between views. Spatially inconsistent predictions across views lead to a weaker response after the outer product, thereby reducing the performance. More importantly, observe that the performance of our 2D approaches is already comparable to most of 3D approaches. This reinforces our claim of working on informative projections at higher resolution being advantageous over working with 3D at lower resolutions.

### C. Effect of adversarial encoding

In addition to the advantages of the Btrfly net, the Btrfly<sub>pe</sub> nets aim to learn the spatial distribution of the vertebrae and encode it into the Btrfly. The contribution of this encoding is observed in the 1–2% improvement over Btrfly’s id. rate. Recall the difference between the *locally* encoding Btrfly<sub>pe-eb</sub> and a more *globally* acting Btrfly<sub>pe-w</sub>. Interestingly, observe that Btrfly<sub>pe-eb</sub>’s performance is marginally superior to Btrfly<sub>pe-w</sub>’s. This can be explained by considering the receptive fields of either of the discriminators: EB-D being fully-convolutional always processes a fixed, local region. W-D, on the other

TABLE I: Performance comparison of our approach (setting  $T = 0$ , for a fair comparison). The reported Id. rate is the mean across three runs of training with different initialisations. However,  $d_{\text{mean}}$  and  $d_{\text{std}}$  are computed over the localisation distances of all vertebrae in the three runs, i.e. over vertebrae in  $3 \times 60$  scans. Improvement in id. rate computed *per scan* across all variants is statistically significant in all runs ( $p < 0.05$ ). Specifically,  $\text{Btrfly}_{\text{pe-eb}}$ 's performance gain is statistically significant with the lowest  $p$ -value  $< 0.001$ .

Approaches	Id. rate (in %)				$d_{\text{mean}}$ ( $d_{\text{std}}$ ) (in mm)			
	All	Cer.	Tho.	Lum.	All	Cer.	Tho.	Lum.
Chen et al. [10]	84.2	91.8	76.4	88.1	8.8 (13.0)	5.1 (8.2)	11.4 (16.5)	8.2 (8.6)
Yang et al. [11]	85	92	81	83	8.6 (7.8)	5.6 ( <b>4.0</b> )	9.2 (7.9)	11.0 (10.8)
Liao et al. [13]	88.3	<b>95.1</b>	84.0	92.2	6.5 (8.6)	<b>4.5</b> (4.6)	7.8 (10.2)	5.6 (7.7)
Cor.+Sag.	85.8 $\pm$ 0.8	92.3 $\pm$ 0.2	80.1 $\pm$ 2.1	90.0 $\pm$ 2.3	6.7 (5.4)	5.8 (5.3)	8.2 (7.4)	7.2 (8.1)
Btrfly	86.7 $\pm$ 0.4	89.4 $\pm$ 0.7	83.1 $\pm$ 1.0	92.6 $\pm$ 1.1	6.3 ( <b>4.0</b> )	6.1 (5.4)	6.9 ( <b>5.5</b> )	5.7 (6.6)
$\text{Btrfly}_{\text{pe-w}}$	87.7 $\pm$ 1.2	89.2 $\pm$ 1.3	85.8 $\pm$ 1.5	<b>92.9<math>\pm</math>1.9</b>	6.4 (4.2)	5.8 (5.4)	7.2 (5.7)	<b>5.6 (6.2)</b>
$\text{Btrfly}_{\text{pe-eb}}$	<b>88.5<math>\pm</math>0.2</b>	89.9 $\pm$ 0.2	<b>86.2<math>\pm</math>0.4</b>	91.4 $\pm$ 1.7	<b>6.2</b> (4.1)	5.9 (5.5)	<b>6.8</b> (5.9)	5.8 (6.6)

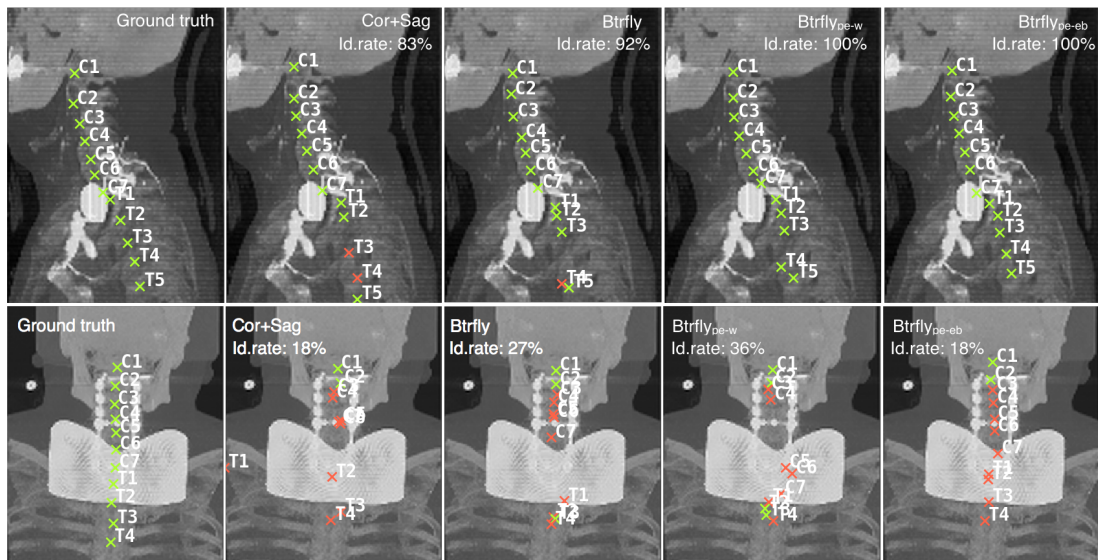


Fig. 5: Qualitative comparison of our network architectures showing two cases with a successful (top, sagittal view) and a failed (bottom, coronal view) labelling. Observe, Cor.+Sag. and Btrfly nets label mostly in presence of spatial information. However, the prior-encoded  $\text{Btrfly}_{\text{pe-x}}$  hallucinate prospective vertebral labels in spite of no image information. Also,  $\text{Btrfly}_{\text{pe-eb}}$  tries to retain the order of vertebral labels.

hand, processes entire scans owing to its dense connections. Since we work with scans of highly varying FOVs, effectively learning and encoding one uniform global prior is non-trivial for W-D. On the other hand, the content in EB-D's receptive field is relatively stable across scans. Moreover, it provides a geometrically-inspired adversarial signal. This difference in encoding also explains the high variance of the id. rates with  $\text{Btrfly}_{\text{pe-w}}$ , which is sensitive to initialisation. Compare this to the stable behaviour of  $\text{Btrfly}_{\text{pe-eb}}$  across initialisations (std 0.2 vs. 1.2). A qualitative comparison of the three variants in our experiments is shown in (Fig. 5). The top row shows a use-case with successful labelling and the bottom rows shows an interesting failure use-case where the labelling fails due to the presence of an obstruction along coronal view.

#### D. Latent space analysis

The latent code of a network is extracted as a channel-wise global mean pooling of the bottleneck layer's feature response. This results in a latent code of length 1024 (or 512 for Cor.+Sag. net). We visualise the two-dimensional t-SNE

representation of the latent space in Fig. 6(a)–(d), obtained on the test set of  $\text{CSI}_{\text{label}}$ . The 2D codes are plotted with the images leading to them.

Since our t-SNE codes are unlabelled, one can expect a distribution dependant only on the image information. Thus, the codes should be clustered loosely into cervical, thoracic, thoracolumbar, and full spine scans. The more distinct these clusters, the more representative the latent space; and smoother the transition between these clusters, more continuous the space. Considering the Cor.+Sag. setup: the coronal network shows a decent segregation for cervical and thoracolumbar spines. However, this is not the case for the sagittal codes. It is due to this disagreement between views that the overall performance goes down. In case of Btrfly, these clusters are more distinct but relatively disjoint, thus preventing a smooth navigation of the space. Compare this with the latent spaces of  $\text{Btrfly}_{\text{pe-w}}$  and  $\text{Btrfly}_{\text{pe-eb}}$ , which are continuous and the transition between clusters is smoother, indicating a representative and continuous space. For understanding how distinct these codes are with respect to each other, we plot the latent codes

TABLE II: The optimal mean  $P$  and  $R$  values based on F1 score, alongside mean of the F1-optimal threshold,  $T$ , in three runs.. Observe that F1-optimal  $R$  of Btrfly<sub>pe</sub> is comparable to state-of-art.

Approach	$T$	$P$	$R$	F1
Cor.+Sag.	0.2	79.5	82.5	79.5
Btrfly	0.33	79.9	85.1	82.4
Btrfly <sub>pe-w</sub>	0.23	77.8	86.1	81.7
<b>Btrfly<sub>pe-eb</sub></b>	0.23	<b>80.2</b>	<b>87.9</b>	<b>83.4</b>

of all the variants obtained from the training set of  $CSI_{label}$  in Fig. 6e. Notice that the Cor.+Sag. net’s codes are very diverse while the rest are relatively clustered.

### E. Precision and Recall

The standard performance measures, viz. id.rate and localisation distances are agnostic to false positive predictions by definition. It is, however, necessary to account for spurious predictions especially when dealing with FCNs, as the predictions depend on a locally constrained receptive field. Therefore, two measures, *precision* ( $P$ ) and *recall* ( $R$ ) were introduced in [19]. It is important to note that id. rate is a *per dataset* measure evaluated over all vertebrae in the test set while  $R$  is measured *per scan* and averaged over all test scans. The latter quantifies success rate for inference on individual scans which is of usual interest. The former is more comprehensive and is of interest in population-studies and the like. As described in Section II-C, in our approach the threshold  $T$  controls the false positive rate. Fig. 7 shows a precision-recall curve generated by varying  $T$  between 0 to 0.8 in steps of 0.1, while Table II records the performance at the F1-optimal threshold. In spite of not choosing a recall-optimistic threshold, our networks perform comparably well at an optimal-F1 threshold. Notice the over-arching nature of Btrfly<sub>pe-eb</sub> over others at all thresholds.

### F. Rigorous evaluation w.r.t Id. rate

As defined in [8], a vertebrae is said to be accurately *identified* if it is the closest to the ground truth and less than 20 mm away. We denote to this distance threshold by  $d_{th}$ . It is noted that  $d_{th} = 20$  mm could be a weaker requirement, e.g. in case of a cervical vertebra which are very close to one another. Demonstrating the spatial precision of our localisation (owing to its ability to work at high resolutions), we perform a breakdown test with respect to the id. rates by varying  $d_{th}$  between 5 mm to 30 mm in steps of 5 mm. Figure 7b shows the region-wise performance curves obtained for this variation across our setups. Notice the reasonably stable behaviour of the curves until  $d_{th} = 10$  mm. This indicates the robustness of our architecture to  $d_{th}$  across regions, i.e a better cervical identification score is not a consequence of a higher  $d_{th}$ . The reduction in the gap between the performance across regions can also be observed from Btrfly to its prior-encoded variants.

## IV. GENERALISABILITY: CLINICAL TRANSLATION

In certain full-body scans, the ribcage obstructs the spine in a naive MIP of the entire scan (Fig. 8b). Additionally,

the spine might not be spatially centred in the sagittal and coronal views. Such cases hinder our algorithm from taking full advantage of Btrfly net’s view-fusion. For handling such cases, we propose a simple pre-processing stage in the form of 3D spine localisation. We argue that incorporating such a stage makes our approach generalisable to any spine scan and also makes the training more stable. We validate our hypothesis by deploying the proposed combination (localisation + Btrfly) on an in-house dataset collected in a clinical setting.

**Dataset.** Our in-house dataset consists of 65 CT scans with voxel-level segmentation. It is a collection of healthy and abnormal spines (e.g. osteoporosis, vertebral fractures, and scoliosis) with the patient ages of 30 years to 80 years collected over two years. At an image level, it has a rich variation of FOVs, scan resolutions, and contrast settings. Of particular interest: 20% of the dataset (13 scans) include the ribcage within the field of view. We believe that the performance of our approach on this dataset closely represents its clinical generalisability. The centroids of the vertebral segmentation masks are considered as vertebral landmarks.

### A. Preprocessing: Spine localisation.

The scans in  $CSI_{label}$  are cropped to a region around spine excluding the ribcage. Thus, naive sagittal and coronal MIPs, without any pre-processing, suffice. On the contrary, the in-house dataset is a mixture of both spine-cropped and full-FOV scans, requiring the use of pre-processing in the form of spine localisation. For localising the spine, we employ a 3D FCN to regress a heat-map around the spine, followed by extracting a bounding box, as in Fig. 8a. In order to avoid clutter, a detailed description of this stage (architecture, inference, and evaluation) is provided in Appendix A. This stage operates at very low resolution (4 mm isotropic resolution), and predicts the *presence* or *absence* of spine as a regression problem. This network is parametrically lean occupying  $\sim 1$ GB on GPU VRAM.

**Improved projections.** As a consequence of localising the spine, we can now extract a *localised* MIP, which is a maximum intensity projection across only those slices that contain the spine in either of the views, thereby resulting in an unoccluded spine. Additionally we extract a weighted and localised *mean* intensity projection (meanIP) by computing a weighted mean along sagittal and coronal views using the localisation’s heatmap as weight. However, in the next section, we see that using just the localised MIP is an optimal choice. Fig. 8b shows a naive MIP with an occluded spine alongside the occlusion-free localised MIP and meanIP.

### B. Experiments

We opt the Btrfly<sub>pe-eb</sub> architecture for this experiment due to its superior performance. We perform a 3-fold cross validation with a split of forty scans for training and twenty-five scans for testing. Convergence is ascertained on a validation set of five scans held out from the training set. We present an ablative comparison in three experiments using: (1) naive MIPs, (2) localised MIP, and finally (3) localised MIPs and meanIP as two inputs. We observe an inferior performance using



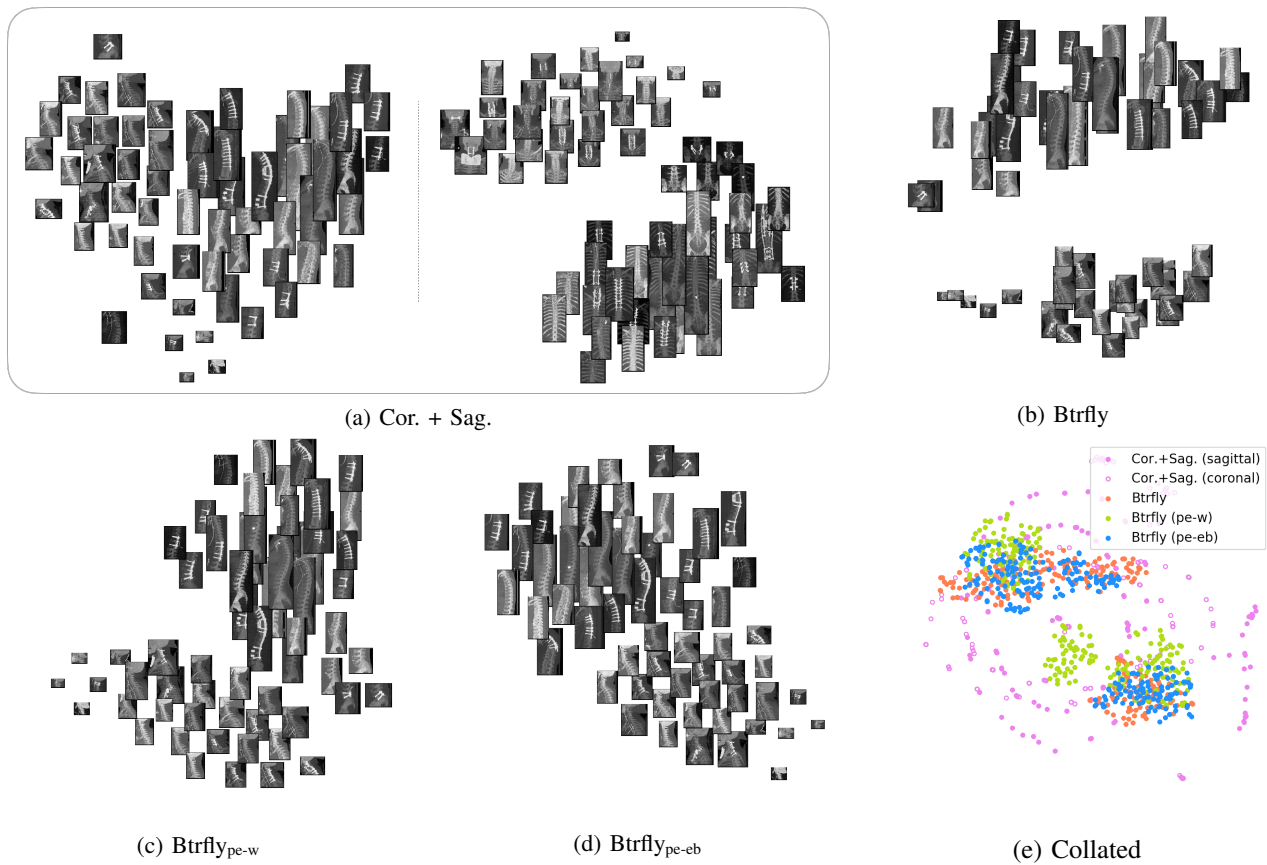


Fig. 6: (a) - (d) t-SNE representations, marked with corresponding input images, representing latent codes of all four experimental setups on test set of  $CSI_{label}$ . (e) Collated t-SNE representation of the variants on the train set of  $CSI_{label}$ . Refer to Section III-D for a detailed analysis of these latent spaces. (Higher resolution version in appendix.)

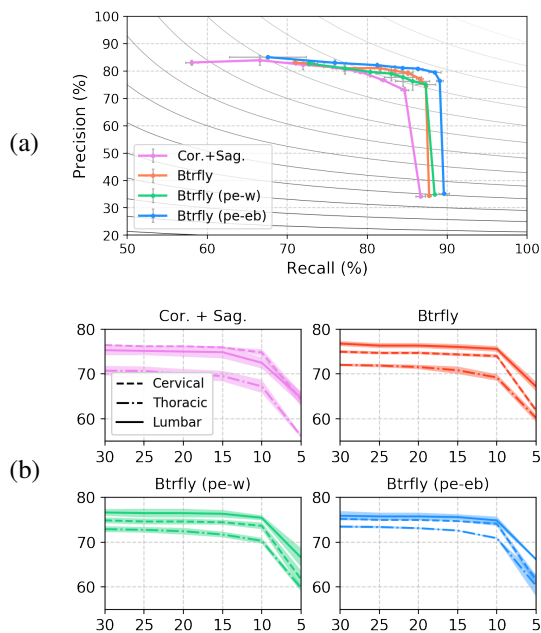


Fig. 7: (a) Precision-recall curve with F1 isolines, illustrating the effect of the  $T$  during inference. For any  $T$ ,  $Btrfly_{pe}$  offers a better trade-off between  $P$  and  $R$ . (b) Region-wise variation of Id. rates (y-axis) for different values of the distance threshold ( $d_{th}$ , x-axis) considered as a *positive identification*.

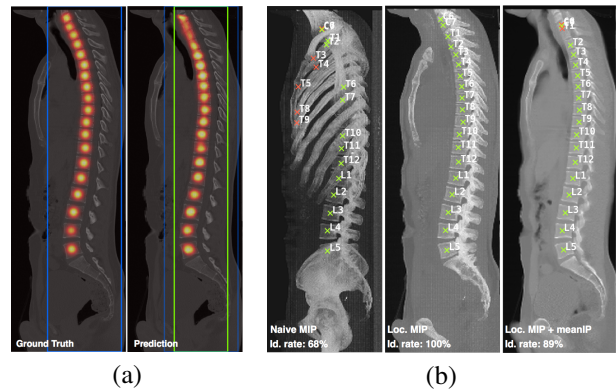


Fig. 8: (a) Spine localisation: Ground truth and predicted heatmaps on mid-slice with extracted bounding boxes (blue and green, respectively). (b) Improved projections alongside naive MIP from the same scan. Observe occlusions in naive MIP and their lack thereof in improved projections. Also illustrated, qualitative performance of  $Btrfly_{pe-eb}$ . Note: Rightmost image is a meanIP but the centroids are predicted using meanIP and localised MIP.

meanIP as a sole input owing to lack of useful key-points in a mean projection. Architecturally, the structure in section III is retained for experiments (1) and (2). However, experiment (3) works with two inputs and needs a slight modification at the input of the two arms of the Btrfly net. In each of the

TABLE III: Btrfly<sub>pe-eb</sub>'s performance on in-house dataset: (I) naive MIP, (II) localised MIP, and (III) localised MIP+meanIP as inputs.

Measures	I	II	III
Id. rate	83.2±1.7	88.0±1.2	82.3±4.0
d <sub>mean</sub> (d <sub>std</sub> )	11.0 (13.0)	8.8 (8.1)	9.5 (8.2)

views, both the reformations are separately processed by a  $3 \times 3$  convolution layer with 32 kernels before being concatenated and fed into the original Btrfly architecture.

**Discussion.** From Table III, observe an inferior id. rate when a naive MIP is employed, due to the spine being occluded. An obviously high d<sub>mean</sub> and d<sub>std</sub> can be observed owing to the lack of visible vertebrae (cf. Fig. 8b). However, localised MIPs from the spine's bounding box results in a relatively uniform input data distribution that is agnostic to FOVs. Its advantage is seen in the 5% gain in id. rate. Interestingly, employing an additional reformation (meanIP) results in an inferior id. rate. This could be attributed to the the distractions induced by soft tissue resulting in the network learning unstable key-points. However, note that d<sub>mean</sub> is comparable to that of localised MIP owing to the spine being un-occluded. Thus, incorrect vertebral labels are not far off from a vertebra. We acknowledge that the introduction of spine localisation invalidates the *end-to-end* feature of our approach. However, highlighting its light weight and accurate performance ( $> 77\%$  intersection-over-union, cf. Appendix A), we recommend its use.

## V. CONCLUSIONS

In this work, we present a novel approach for labelling the vertebrae using sufficiently informative 2D orthogonal projections of the spine. Our architecture, called the Btrfly net, combines information across sagittal and coronal maximum intensity projections. Augmenting this, we propose two distinct adversarial training regimes for the Btrfly net so as to encode an anatomical prior into it. An energy-based adversarial training scheme encodes a *local* vertebral spread, while a Wasserstein-distance based one tries to encode a more *global* prior corresponding to the full spine. As our results suggest, albeit prior-encoding in any form improves performance, for our task of vertebrae labelling, a local encoding performs better. This is owing to its stability of the local-structure across scans and to its geometric motivation. The performance of an adversarially-trained Btrfly net with an energy-based discriminator is comparable to prior state-of-art approaches while working in 2D and being a stand-alone network. In translating our approach to clinical settings, we show that introducing a simple spine pre-localisation stage subdues the variability in input data thereby making our approach more robust.

## REFERENCES

- [1] J. A. Cauley, D. E. Thompson, K. C. Ensrud, J. C. Scott, and D. Black, "Risk of mortality following clinical fractures," *Osteoporosis Int.*, vol. 11, no. 7, pp. 556–561, 2000.
- [2] A. C. Papageorgiou, P. R. Croft, E. Thomas, S. Ferry, M. I. Jayson, and A. J. Silman, "Influence of previous pain experience on the episode incidence of low back pain: results from the south manchester back pain study," *Pain*, vol. 66, no. 2-3, pp. 181–185, 1996.
- [3] S. H. Gehlbach, C. Bigelow, M. Heimisdottir, S. May, M. Walker, and J. R. Kirkwood, "Recognition of vertebral fracture in a clinical setting," *Osteoporos Int*, vol. 11, no. 7, pp. 577–582, 2000.
- [4] S. Schmidt, J. Kappes, M. Bergholdt, V. Pekar, S. Dries, D. Bystrov, and C. Schnörr, "Spine detection and labeling using a parts-based graphical model," in *Information Processing in Medical Imaging*. Springer, 2007.
- [5] T. Klinder, J. Ostermann, M. Ehm, A. Franz, R. Kneser, and C. Lorenz, "Automated model-based vertebra detection, identification, and segmentation in ct images," *Medical Image Analysis*, vol. 13, no. 3, pp. 471–482, 2009.
- [6] J. Ma and L. Lu, "Hierarchical segmentation and identification of thoracic vertebra using learning-based edge detection and coarse-to-fine deformable model," *Comput. Vis. Image Underst.*, vol. 117, no. 9, pp. 1072–1083, 2013.
- [7] B. Glocker, J. Feulner, A. Criminisi, D. R. Haynor, and E. Konukoglu, "Automatic localization and identification of vertebrae in arbitrary field-of-view ct scans," in *Medical Image Computing and Computer-Assisted Intervention*. Springer, 2012.
- [8] B. Glocker, D. Zikic, E. Konukoglu, D. R. Haynor, and A. Criminisi, "Vertebrae localization in pathological spine ct via dense classification from sparse annotations," in *Medical Image Computing and Computer-Assisted Intervention*. Springer, 2013.
- [9] A. Suzani, A. Seitel, Y. Liu, S. Fels, R. N. Rohling, and P. Abolmaesumi, "Fast automatic vertebrae detection and localization in pathological ct scans - a deep learning approach," in *Medical Image Computing and Computer-Assisted Intervention*. Springer, 2015.
- [10] H. Chen, C. Shen, J. Qin, D. Ni, L. Shi, J. C. Y. Cheng, and P.-A. Heng, "Automatic localization and identification of vertebrae in spine ct via a joint learning model with deep neural networks," in *Medical Image Computing and Computer-Assisted Intervention*. Springer, 2015.
- [11] D. Yang, T. Xiong, D. Xu, Q. Huang, D. Liu, S. K. Zhou, Z. Xu, J. Park, M. Chen, T. D. Tran *et al.*, "Automatic vertebra labeling in large-scale 3d ct using deep image-to-image network with message passing and sparsity regularization," in *Information Processing in Medical Imaging*. Springer, 2017.
- [12] D. Yang, T. Xiong, D. Xu, S. K. Zhou, Z. Xu, M. Chen, J. Park, S. Grbic, T. D. Tran, S. P. Chin *et al.*, "Deep image-to-image recurrent network with shape basis learning for automatic vertebra labeling in large-scale 3d ct volumes," in *Medical Image Computing and Computer-Assisted Intervention*. Springer, 2017.
- [13] H. Liao, A. Mesfin, and J. Luo, "Joint vertebrae identification and localization in spinal ct images by combining short- and long-range contextual information," *IEEE Transactions on Medical Imaging*, vol. 37, no. 5, pp. 1266–1275, 2018.
- [14] H. Ravishankar, R. Venkataramani, S. Thiruvankadam, P. Sudhakar, and V. Vaidya, "Learning and incorporating shape models for semantic segmentation," in *Medical Image Computing and Computer Assisted Intervention*. Springer, 2017.
- [15] O. Oktay, E. Ferrante, K. Kamnitsas, M. P. Heinrich, W. Bai, J. Caballero, R. Guerrero, S. A. Cook, A. de Marva, T. Dawes *et al.*, "Anatomically constrained neural networks (ACNN): application to cardiac image enhancement and segmentation," *CoRR*, vol. abs/1705.08302, 2017.
- [16] I. Goodfellow, J. Pouget-Abadie, M. Mirza, B. Xu, D. Warde-Farley, S. Ozair, A. Courville, and Y. Bengio, "Generative adversarial nets," in *Advances in Neural Information Processing Systems 27*, 2014.
- [17] M. Arjovsky, S. Chintala, and L. Bottou, "Wasserstein GAN," *CoRR*, vol. abs/1701.07875, 2017.
- [18] J. Zhao, M. Mathieu, and Y. LeCun, "Energy-based Generative Adversarial Network," *CoRR*, vol. abs/1609.03126, 2016.
- [19] A. Sekuboyina, M. Rempfler, J. Kukačka, G. Tetteh, A. Valentinitich, J. S. Kirschke, and B. H. Menze, "Btrfly net: Vertebrae labelling with energy-based adversarial learning of local spine prior," in *Medical Image Computing and Computer Assisted Intervention*. Springer, 2018.
- [20] I. Gulrajani, F. Ahmed, M. Arjovsky, V. Dumoulin, and A. C. Courville, "Improved training of wasserstein gans," in *Advances in Neural Information Processing Systems 30*, 2017.
- [21] M. Lucic, K. Kurach, M. Michalski, S. Gelly, and O. Bousquet, "Are GANs Created Equal? A Large-Scale Study," *CoRR*, vol. abs/1705.08302, 2017.
- [22] K. He, X. Zhang, S. Ren, and J. Sun, "Spatial Pyramid Pooling in Deep Convolutional Networks for Visual Recognition," *CoRR*, vol. abs/1406.4729, 2014.

APPENDIX A  
PRE-PROCESSING: SPINE LOCALISATION

A. Architecture

For completeness, we briefly discuss the learning procedure involved for localising the spine. For this task, annotations can be obtained from the available vertebral centroids as a maximum along the channels of  $y$ , viz.  $\max_i(y_i)$ . The input is a 3D scan at low isotropic resolution of 4 mm. The output is also a 3D volume with a Gaussian at every vertebra location. Owing to lower resolution and to simplify the localisation task, we use a higher  $\sigma$  (=15) for wider Gaussians as annotations.

These annotations are learnt with a very light-weight fully-convolutional U-network. Fig. 9 gives a detailed overview of the architecture. Once trained, the network predicts a ‘heat-map’ (values between 0 and 1) that indicates the location of the spine. Fig. 10 shows to use cases processed with our localisation network. Note that we extract a bounding box once the spine is localised. For this, we nullify all the values below 0.5 and consider the lowest and the highest coordinate of an active voxels in the coronal and sagittal direction. Padding these bounding voxels by a fixed value on all four sides, we construct a bounding box. Once the bounding box is extracted we could proceed with the extraction of localised mean intensity projections.

B. Evaluation

It is important to realise that it suffices to localise the spine just so that the obstructions in the projections are eliminated. Thus, we do not impose demanding performance standards for this stage. We evaluate the localisation with two metrics, one of them modestly lenient, as defined:

- 1) *Intersection-over-union* (IoU) between the actual bounding box and the bounding box obtained from the prediction. We report the mean IoU over the test set.
- 2) *Detection rate*, where a detection is successful if the corresponding IoU of greater than 50%. It was observed that the vertebrae is distinguishable in the projections within this tolerance of IoU.

Table IV records the performance of this stage on the two datasets used in our work:  $CSI_{label}$  and the in-house datasets. A detection rate of 1.0 indicates a successful localisation of the spine in all the cases with a tolerable overlap. It was observed that this overlap suffices for our task of filtering out the obstructions.

TABLE IV: Performance of the localisation on the three datasets. Detection rate indicates the reliability of the localisation stage in constructing inputs for the next stage of labelling.

Measures	$CSI_{label}$	In-house
Mean IoU	0.86	0.77
Detection rate	1.0	0.96

APPENDIX B  
ADDITIONAL ILLUSTRATIONS

In Fig. 11, We visualise t-sne plots from Fig. 6 of the main manuscript at a higher resolution so that the transition

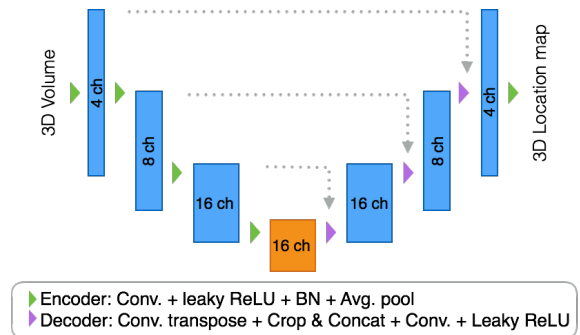


Fig. 9: Localisation network’s architecture. Kernel sizes: All convolution kernels except the last layer are  $3 \times 3 \times 3$ . Last convolutional kernel is  $1 \times 1 \times 1$ . Transposed convolution kernels are  $4 \times 4 \times 4$ . Average pooling kernels are  $2 \times 2 \times 2$  with a stride of 2 in all directions.

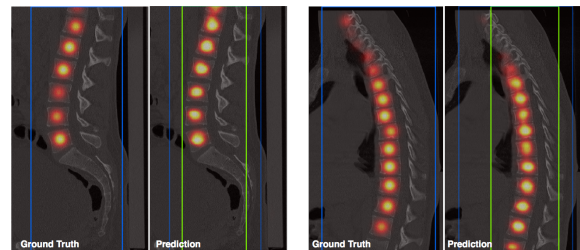


Fig. 10: Ground truth and predicted localisation maps along with extracted bounding boxes (Blue – actual, Green – predicted), plotted on mid sagittal slices of the scan.

across various field-of-views can be better appreciated. In each case, observe the segregation of the images into three soft clusters: the cervical, thoracic and the thoracolumbar scans. The smoother the transition between these clusters, the smoother the latent space (as observed in  $Btrfly_{pe-eb}$  and  $Btrfly_{pe-w}$ ). In Fig. 12, we also illustrate a few additional qualitative results from  $CSI_{label}$  dataset at a higher resolution.

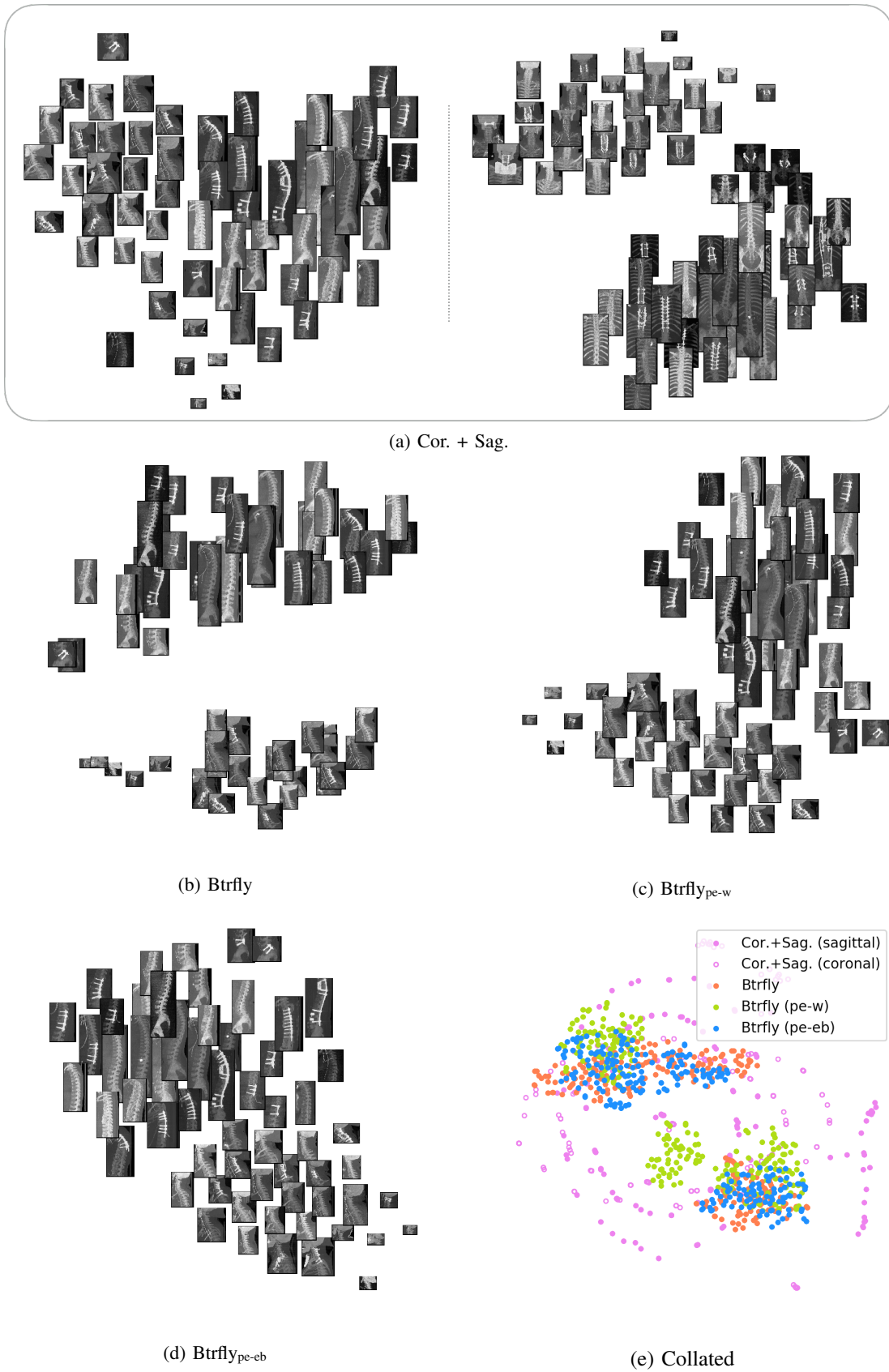


Fig. 11: (a) - (d) t-SNE representations, marked with corresponding input images, representing latent codes of all four experimental setups on test set of  $CSI_{label}$ . (e) Collated t-SNE representation of the variants on the train set of  $CSI_{label}$ . Refer to Section III-D for a detailed analysis of these latent spaces.

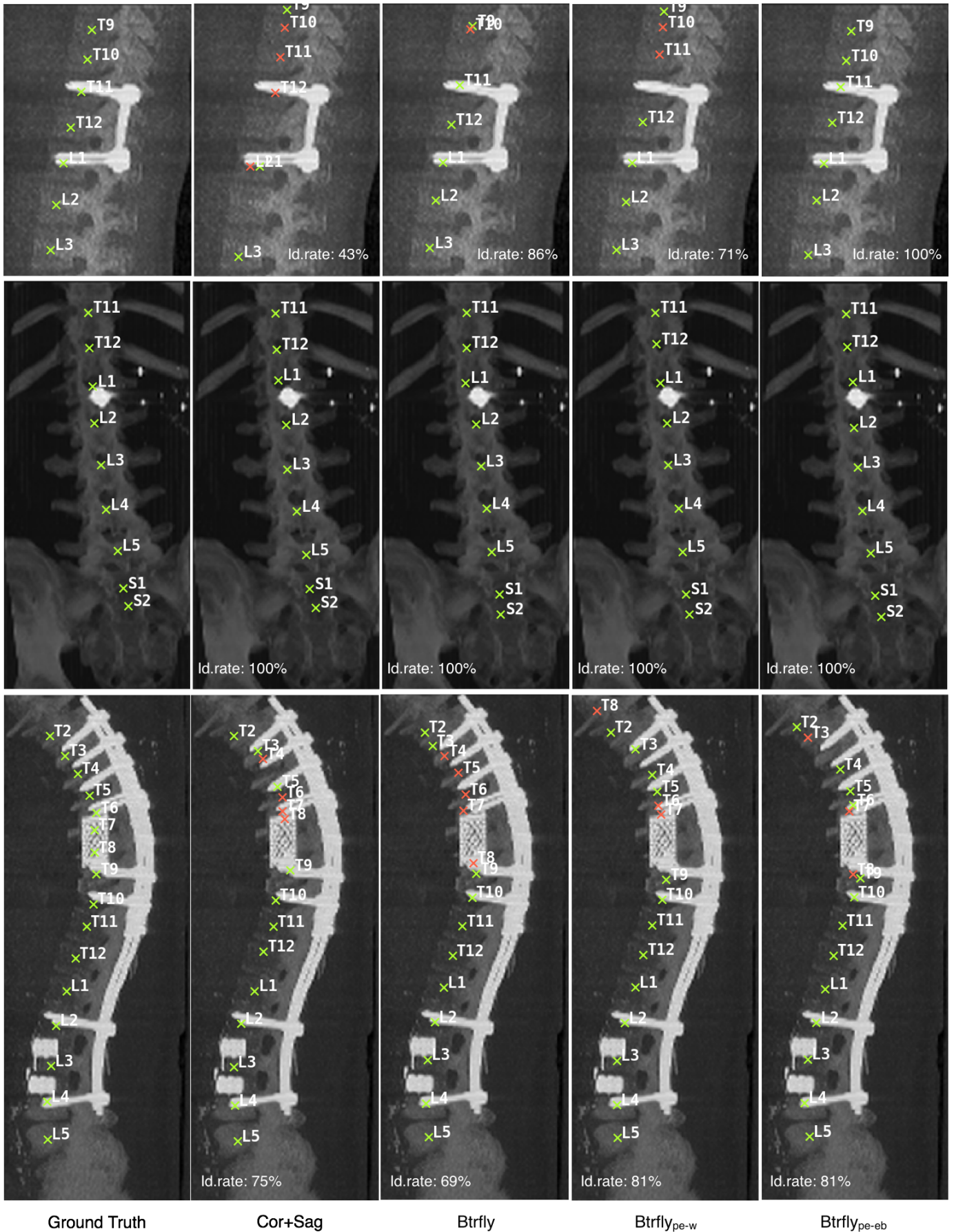


Fig. 12: Additional qualitative results on the CSI<sub>label</sub> dataset showing the labels on both sagittal and coronal reformations. Notice the ability to our 2D networks to accurately label the vertebrae in 3D in spite of an extreme loss of spatial information due to metal insertions.